Above-band-gap dielectric functions of ZnGeAs_{2}: Ellipsometric measurements and quasiparticle self-consistent GW calculations

S. G. Choi, M. van Schilfgaarde, D. E. Aspnes, A. G. Norman, J. M. Olson, T. J. Peshek, and D. H. Levi

Phys. Rev. B **83**, 235210 — Published 15 June 2011

DOI: 10.1103/PhysRevB.83.235210

Above-Bandgap Dielectric Functions of $ZnGeAs_2$:

Ellipsometric Measurements and Quasiparticle Self-consistent GW Calculations

S.G. Choi,[1,a] M. van Schilfgaarde,[2] D.E. Aspnes,[3] A.G. Norman,[1] J.M. Olson,[1] T.J. Peshek,[1,2,b] and D.H. Levi[1]

[1] *National Renewable Energy Laboratory, Golden, Colorado 80401, USA*

[2] *School for Engineering of matter, transport and energy, Arizona State University, Tempe, Arizona 85287, USA*

[3] *Department of Physics, North Carolina State University, Raleigh, North Carolina 27695, USA*

ABSTRACT

We report the above-bandgap dielectric function spectra $\varepsilon_a = \varepsilon_{a1} + i\varepsilon_{a2}$ of single-crystal $ZnGeAs_2$ grown epitaxially on (001)GaAs, and study it theoretically. After surface overlayers were removed chemically to minimize artifacts, pseudodielectric-function spectra $\langle\varepsilon\rangle = \langle\varepsilon_1\rangle + i\langle\varepsilon_2\rangle$ were acquired ellipsometically from 1.5 to 6.0 eV with the sample at room temperature. The ε_a spectra were then extracted by the multilayer analysis. The procedure ensures that the result is a close approximation to the *a*-axis component of the dielectric-function tensor $\varepsilon = \varepsilon_1 + i\varepsilon_2$ of $ZnGeAs_2$. The data exhibit numerous spectral features associated with critical points. The energies of these critical points are determined accurately by fitting standard lineshapes to second energy derivatives of the data obtained by a combined method of spectral analysis. We compare our results to the predictions of quasiparticle self-consistent *GW* calculations. Good agreement is achieved for the major critical-point features, and their probable origins are identified.

---

[a] Author to whom correspondence should be addressed; electronic mail: Sukgeun.Choi@nrel.gov

[b] Present affiliation: eQED, LLC., Mayfield Village, Ohio 44143, USA.

I. INTRODUCTION

The II-IV-V_2 chalcopyrite-phase ternary compound $ZnGeAs_2$ is the logical extension of the III-V binary compound GaAs, where the Zn and Ge reside at adjacent Ga sites in an ordered manner.[1] Because its 1.15 eV bandgap is direct and its *in-plane* lattice parameter is close to that of (001)GaAs, $ZnGeAs_2$ layers can be incorporated into the conventional $Ga_{0.52}In_{0.48}P$/GaAs/Ge three-junction solar-cell structure to allow more efficient capture of incoming photons without compromising lattice structure. As a result, $ZnGeAs_2$ is a promising constituent for high-efficiency III-V-multijunction solar cells.[2,3] In addition, a newly proposed tandem-cell concept[4] based on $ZnGeAs_2$ and related II-IV-V_2 compounds is revitalizing interest in this material.

Knowledge of the optical response of solids, for example the dielectric function $\varepsilon = \varepsilon_1 + i\varepsilon_2$ and refractive index $N = n + ik = \sqrt{\varepsilon}$, is necessary for the design and development of high-performance photonic and photovoltaic devices.[5] Even though a limited number of reflectance spectra of $ZnGeAs_2$ are available,[6-10] ε and N data are rare. The ε spectra reported in Ref. 10 were calculated indirectly by a Kramers-Kronig (K-K) transform of low-temperature (80 K) reflectance data of polycrystalline $ZnGeAs_2$. The results are therefore a mix of the two components of the dielectric-function tensor of this optically uniaxial material. In addition, it is well known[11] that K-K analysis of reflectance data may lead to systematic errors, so an independent determination is justified.

To obtain our data we use spectroscopic ellipsometry (SE). SE is a nondestructive optical technique[11] that can determine ε and N accurately over a wide range of photon energies without need of K-K analysis. As a result, SE has been widely used to study optical properties of many semiconductors in the past few decades.[12] Our data concern the intrinsic ε of a $ZnGeAs_2$ thin film grown epitaxially on GaAs. Since $ZnGeAs_2$ grows with its c axis normal to the surface and SE measurements are dominated by the component(s) of the ε tensor perpendicular to the c axis (here parallel to the measurement surface),[13,14] our data are a close approximation to the component ε_a of ε. This is the component relevant for normal-incidence illumination. We compare our data to the predictions of quasiparticle self-consistent *GW* calculations.[15] We also report accurate values of the CP energies, which we determine by a combined method of spectral analysis.[16] Finally, we use the approximate self-consistent electronic-structure method to identify the probable origins of the CP features.

II. EXPERIMENT

A 200-nm film of chalcopyrite-phase $ZnGeAs_2$ was grown epitaxially on a lattice-matched $Ga_{0.52}In_{0.48}P$ buffer layer on a 6° B-miscut GaAs(001) substrate by low-pressure (50 Torr) metalorganic vapor phase epitaxy. The nominal thickness of the $Ga_{0.52}In_{0.48}P$ buffer layer was 250 nm. The sources were arsine, germane, and diethylzinc. Chalcopyrite $ZnGeAs_2$ grows only under a very narrow range of conditions.[17] More generally, body-centered tetragonal Zn_3As_2 forms instead, which is lattice-mismatched to GaAs and hence contains a high-density of dislocations.

We confirmed the chalcopyrite phase with transmission electron diffraction (TED) using a Philips CM30 transmission electron microscope (TEM) operating at 300 kV. The pattern shown in Fig. 1(a) was obtained from a plan-view TEM sample of the $ZnGeAs_2$ layer, tilted to what would be the [111] pole for the zincblende structure. The arrow indicates the array of extra spots that do not occur for zincblende material, but which are in excellent agreement with the calculated pattern for the [111] pole of chalcopyrite $ZnGeAs_2$. Energy dispersive x-ray microanalysis (EDX) data (not shown) verify the presence of Zn, Ge, and As at the expected ratios within experimental uncertainty. Additionally, the [110] high-resolution cross-section TEM image given in Fig. 1(b) shows a defect-free interface between epitaxial $ZnGeAs_2$ and $Ga_{0.52}In_{0.48}P$ as well as the high crystalline quality of $ZnGeAs_2$ film.

SE data were acquired from 1.5 to 6.0 eV using an automatic spectroscopic rotating-compensator ellipsometer operating at an angle of incidence of 67.08°. The polarizer and analyzer azimuths were both set to 30°, and a 504-µm-thick MgF_2 monoplate was used as the compensator. The sample was optically prealigned and maintained in a windowless cell under flowing purified N_2. This unique configuration[18] enabled us to chemically strip the surface overlayers while monitoring the effectiveness of the cleaning procedure in real time. Our sequence consisted of deionized (DI) water, methanol, a 50 vol. % solution of NH_4OH in DI water (AmH) followed by DI water rinse, and a 0.01 vol. % solution of Br in methanol (BrM) followed by a methanol rinse. Chemical treatments were repeated until the SE data showed no further changes, which is indicative of a flat surface with a minimal overlayer.[18]

Effects of chemical treatments on the $\langle \varepsilon_2 \rangle$ spectrum of $ZnGeAs_2$ are shown in Fig. 2(a). The significant increase in the value of $\langle \varepsilon_2 \rangle$ in the 4 to 5 eV range indicates the removal of a fairly thick surface overlayer[19] in accordance with previous studies.[18,20] The effect of the initial DI water rinse (not shown in Fig. 2(a)) is strongly positive, suggesting that a major component of the surface overlayer is a Ge-related oxide. Oxides related to As were removed by AmH, and Zn-related oxides and other residues (including microscopic roughness) were removed by BrM.[18]

A side benefit of these treatments is that several optical structures are better resolved. Structure in the spectral range below about 2 eV is slightly blue-shifted after exposure to BrM, which suggests that the associated features are due to interference, and that BrM removes not only overlayers but also the top few layers of $ZnGeAs_2$.

The positive effects of the AmH treatment were confirmed by X-ray photoemission spectroscopy (XPS). Figure 2(b) shows XPS spectra acquired in a Physical Electronics 5600 photoemission system using monochromatic Al Kα radiation, a 45° take-off angle, and an 800 μm slit. The pass energy was 29.35 eV and the dwell time per data point was 2 sec. Compared to the XPS data for surface rinsed with DI water (solid green line), those for the AmH treated surface (solid red line) show a significant enhancement of the Zn $2p_{3/2}$ peak intensity at 1022 eV as well as the disappearance of the "overlayer" peak. This demonstrates the effectiveness of the AmH treatment. As shown in the inset of Fig. 2(b), AmH treatment also reduces the amount of C-related contaminants on the $ZnGeAs_2$ surface.

As a reference, the XPS spectrum for the surface prepared by in-situ Ar sputtering (solid black line) is included in Fig. 2(b). Here, the surface was processed by a 1 keV Ar^+ beam with a current density of 6 μA/cm^2. Even though the AmH treatment does not fully compete with in-situ sputter cleaning, it eliminates a major fraction of surface contamination. In fact, sputtering can lead to phase segregation in addition to causing near-surface damage, which potentially adversely affects the optical data.[11] Therefore, the in-situ wet-etching procedures described here enabled us to minimize overlayer artifacts and hence to obtain a close approximation to the intrinsic optical functions of $ZnGeAs_2$.

III. QUASIPARTICLE SELF-CONSISTENT *GW* (QS*GW*) CALCULATIONS

The electronic energy band structure of $ZnGeAs_2$ calculated within the QS*GW* approximation[15] is presented in Fig. 3. The ε spectra along the two principal axes *a* and *c* were also calculated within the random phase approximation (RPA)[21] and compared to the SE data, to be discussed in Sec. IV. The local density approximation (LDA) to density functional theory (DFT) has been widely used for these purposes, but the LDA-DFT approach tends to underestimate semiconductor bandgaps ("LDA gap error") and describes conduction-band dispersion poorly.

The QS*GW* approximation used in this study is a new first-principles method of solving the Schrödinger equation within Hedin's *GW* theory.[22] This approach essentially uses the low-order terms in many-body perturbation theory. Because it is an expansion about a non-interacting Hamiltonian H_0, the calculated band structure depends strongly on the choice of H_0. Standard implementations of *GW* use the LDA to construct H_0. However, this procedure suffers from underestimating semiconductor band gaps, and the amount of underestimation varies from one semiconductor to another. In the QS*GW*, self-consistency is used to select a H_o as close as possible to the full interacting Hamiltonian *H*. The QS*GW* is an internally consistent scheme that no longer depends on the LDA.

The QS*GW* approximation is highly reliable, and is sufficiently accurate to predict key properties over a wide range of materials systems. Even though small errors occur, these are systematic and understandable. In the present context, the predominant error arises from the RPA used in the ε calculations. Electron-hole excitations in the virtual states are included only in the time-dependent

Hartree approximation (also known as RPA), leaving out the contributions from the attractive interactions. Therefore, the peaks in the ε_2 spectrum appear at energies higher than those observed. As can be seen from the K-K relations connecting the ε_1 and ε_2, this error results in a systematic underestimation of ε_∞. This leads in turn to a slight overestimation of the $W(\omega \rightarrow 0)$ that is the predominant contribution to the *GW* self-energy, since it scales as $1/\varepsilon_\infty$. As a consequence, the bandgap energies are overestimated by about 0.2 to 0.3 eV for many III-V semiconductors.[21]

In principle, we can reduce the above problems by including the electron-hole attraction in the calculations through the ladder diagram,[23] although this procedure is costly in practice. Given that ε_∞ is systematically overestimated by a universal factor of 0.8, a simple solution is to scale $\Sigma = iGW$ by 0.8.[21] With this correction, the bandgap energies for many semiconductors and insulators are described very accurately with a gap error typically less than 0.1 eV.

The QS*GW* gap for $ZnGeAs_2$ is estimated to be 1.3 eV, but the scaling procedure described above reduced it to 1.1 eV. Although the differences are relatively small, we present the band structure with the scaled Σ to obtain a band structure that is as accurate as possible.

IV. RESULTS AND DISCUSSION

Our best $ZnGeAs_2$ $<\varepsilon>$ data, shown in Fig. 2(a), were further analyzed by a multilayer model consisting of the ambient, a surface-roughness layer, the $ZnGeAs_2$ layer, the $Ga_{0.52}In_{0.48}P$ buffer layer, and the GaAs substrate as shown in the inset of Fig. 4. Because the *c*-axis contribution is minor, we ignore the anisotropic nature of $ZnGeAs_2$. We analyzed the $<\varepsilon>$ data by using the known optical functions of bulk $Ga_{0.52}In_{0.48}P$ and GaAs[18] and representing the $ZnGeAs_2$ spectrum with nine Gaussian oscillators. We estimated the surface-roughness layer to be ~ 0.25 nm thick, and modeled its response as a Bruggeman effective-medium-approximation (BEMA)[24,25] 50-50 mixture of the $ZnGeAs_2$ layer and void. The ellipsometric data Ψ and Δ, and their best-fit curves are shown as the open symbols and solid lines, respectively, in Fig. 4. Model and data are in excellent agreement. Only 20% of the actual data points are presented here to show clearly the quality of fit.

The ε data that we obtained are given in Table I. The spectra themselves are shown in Fig. 5(a), along with ε spectra calculated for the polarization field perpendicular (ε_a) and parallel (ε_c) to the *c* axis. The SE results are given as solid lines, and the calculations for the ε_a and ε_c as dotted and dashed lines, respectively. By comparing Figs. 2a and 5a, we see that most spectral features are preserved whereas the interference oscillations below 2 eV are eliminated.

As seen in Fig. 5(a), $ZnGeAs_2$ exhibits many CP features, more than its III-V counterpart, GaAs. This is partly due to the difference in atomic structure. Since the Brillouin-zone (BZ) volume of chalcopyrite is 4 times smaller than that of zincblende, there is a 4-to-1 mapping of energy levels of the zincblende BZ into the chalcopyrite BZ.[1] As a result, the energy band structure and related optical functions of chalcopyrite crystals are complicated. In addition, the selection rules are somewhat relaxed for the lower symmetry. Thus, some of the transitions that forbidden in GaAs are allowed for $ZnGeAs_2$.[7]

The agreement between the data and calculated ε_a spectrum is reasonable. All the pronounced CP structures observed in ε_2 are identified in the QS*GW* results, as indicated in Fig. 5(b) by the arrows. The difference of ~ 0.5 eV in the CP energies between data and calculation is expected, since the RPA calculations consider the electron-hole interactions in the virtual excitations whereas the data actually contain many-body effects. The second discrepancy is that the calculations underestimate the magnitude of ε_2 in the region below about 4 eV and overestimate it above about 5 eV. Discrepancies in the predicted energies and amplitudes of CP structures are commonly seen in these calculations.[26] Despite these differences, the peaks in the QS*GW* spectrum accurately reflect the splittings in the quasiparticle (QP) levels, i.e., the differences between unoccupied and occupied states. The good agreement between the SE-determined ε data and the calculated ε_a spectrum also validates the argument that the SE-determined ε data are a good approximation to the ordinary component ε_a of the dielectric tensor for $ZnGeAs_2$.

To obtain energies of the CP structures observed in Fig. 5, we used a newly developed combined method of spectral analysis.[16] First, we Fourier-transformed the *pseudodielectric function* $<\varepsilon_1>$ and $<\varepsilon_2>$ data, shown in Fig. 2, to generate the reciprocal-space (RS) coefficients $C_n e^{i\xi_n}$, where C_n and ξ_n are the amplitude and phase, respectively, of the n^{th} coefficient.[27] The advantage in doing this is that baseline, information, and noise are separated in the $C_n e^{i\xi_n}$. These coefficients were then filtered with a high-index Gaussian cutoff. The direct-space second-derivative spectra were then reconstructed from these filtered coefficients. Use of the second derivative is advantageous for two reasons. First, it provides the filtering needed to suppress baseline effects. Second, its construction requires most of the intermediate-index coefficients, and hence it makes highly efficient use of CP information. Standard CP expressions were then least-squares fit to the reconstructed derivatives. These standard expressions are[28,29]

$$\frac{d^2\varepsilon}{dE^2} = \begin{cases} n(n-1)Ae^{i\phi}(E - E_g + i\Gamma)^{n-2}, n \neq 0 \\ Ae^{i\phi}(E - E_g + i\Gamma)^{-2}, n = 0 \end{cases} , \qquad (1)$$

where A is the amplitude, E_g is the threshold energy, Γ is the broadening parameter, and ϕ is the excitonic phase angle. For $A > 0$, the values $n = -1, -1/2, 0$, and $1/2$ represent excitonic, one-, two-, and three-dimensional lineshapes, respectively. Both real and imaginary parts were fit simultaneously.

The open circles and squares in Fig. 6 represent the reconstructed $d^2<\varepsilon_1>/dE^2$ and $d^2<\varepsilon_2>/dE^2$ spectra, respectively. For clarity, the number of data points (symbols) was reduced by half. The solid and dash-dotted lines are the best-fit curves to the real and imaginary parts, respectively, using the excitonic lineshape $n = -1$. A total of eight critical-points lineshapes were needed to analyze the spectrum from 2 to 5.25 eV. The CP energies obtained are listed in Table II. The labeling follows that of a previous room-temperature reflectance study.[7] For comparison, the CP energies[6-10,30] previously reported are also included.

To understand the origin of each CP structure, we calculated several ε_2 spectra, resolving the contributions from particular valence bands using the approximate self-consistent electronic-structure method. Zincblende GaAs has 4 valence bands when spin-orbit coupling is not included. In principle, chalcopyrite $ZnGeAs_2$ has 16 valence bands because it has 4 times more atoms per unit cell than GaAs. In addition, two of these atoms are Zn, which have 3*d* states. These add another 10 bands. Therefore, we considered a system consisting of 52 electrons in a total of 26 bands for our calculations. However, the additional ten 3*d* bands are very deep and reside about 8 ~ 9 eV below the valence band maximum. To make the comparison with GaAs simpler, we conceptually regarded them as the core bands and assigned number 16 to the uppermost valence band. Figures 7(a) through 7(f) show the ε_2 spectra resulting from the individual valence bands 11 through 16 to separate conduction bands (colored lines), then to all available conduction bands (dashed lines).

For zincblende semiconductors the dominant CP features are due to transitions localized at or near high-symmetric points of the BZ, such as Γ, L, and X. The corresponding locations for the chalcopyrite structures are Γ, N, and T (see Fig. 3). The E_1, E_2, and E_3 CPs of $ZnGeAs_2$ shown in Fig. 5 are analogous to the E_1 and E_1+Δ_1 CPs for GaAs, and occur in the vicinity of the N points.[8] Figures 7(e) and 7(f) suggest that these CP structures are primarily due to transitions from the 15th and 16th valence bands to the 1st and 2nd conduction bands. The E_4 CP of $ZnGeAs_2$ does not have a GaAs counterpart, and this structure has been attributed to the transitions along the F line between the Γ and N points.[8] Transitions from the 16th valence band to the 3rd and 4th conduction bands are responsible for this CP structure, as suggested in Fig. 7(f). The higher-energy CPs of $ZnGeAs_2$ are analogous to the E_0' and E_2 CPs of GaAs, and seem to have multiple contributions as revealed in Figs. 7. The major contributions to each CP structure are summarized in Table II.

V. CONCLUSION

SE has been used to determine the component ε_a of the dielectric-function tensor of chalcopyrite $ZnGeAs_2$, where ε_a is the component of ε perpendicular to the *c* axis. We used in situ wet chemical etching to obtain the $<\varepsilon>$ data least affected by surface overlayers and then obtained ε spectrum using the multilayer analysis, which is thus most closely related to ε_a. Our $<\varepsilon>$ data exhibit 8 CP structures from 2 to 5.25 eV, and their energies are obtained accurately by the combined method of spectral analysis. The data show good agreement with the $\varepsilon_\perp$ spectrum calculated in the quasiparticle self-consistent *GW* approximation. In addition, we calculated $\varepsilon_\perp$ using the approximate method of self-consistent electronic structure to obtain the separate contributions of the uppermost 6 valence bands, so that we can better elucidate possible origins of these features.

ACKNOWLEDGMENTS

This work was supported by the U.S. Department of Energy (DOE) under Contract No. DE-AC36-08GO28308. The work done at the Arizona State University was supported by the U.S. DOE under Grant No. DE-FG36-08GO18002. The authors gratefully acknowledge C.L. Perkins of the National Renewable Energy Laboratory for X-ray photoemission spectroscopic measurements. The optical data of $Ga_{0.52}In_{0.48}P$ bulk were kindly provided by J.A. Woollam Co., Inc.

REFERENCES

[1] U. Kaufmann and J. Schneider, in *Advances in Solid State Physics*, Edited by H.J. Queisser (Pergamon, Oxford, 1974) Ch. 14.

[2] S.R. Kurtz, D. Myers, and J.M. Olson, in *Proceedings 26th IEEE Photovoltaics Specialist Conference* (IEEE, New York, 1997), p. 875.

[3] A. Janotti, S.-H. Wei, S.B. Zhang, and S. Kurtz, Phys. Rev. B **63**, 195210 (2001).

[4] M. van Schilfgaarde, T.J. Coutts, N. Newman, and T. Peshek, Appl. Phys. Lett. **96**, 143503 (2010).

[5] M. Law, M.C. Beard, S. Choi, J.M. Luther, M.C. Hanna, and A.J. Nozik, Nano Lett. **8**, 3904 (2008).

[6] C.C.Y. Kwan and J.C. Woolley, Can. J. Phys. **48**, 2085 (1970).

[7] V.I. Donetskich, A.S. Poplavnoi, and V.V. Sobolev, Phys. Stat. Solidi (b) **48**, 541 (1971).

[8] G.Z. Krivaite and A. Yu. Shileika, Sov. Phys. Semicon. **7**, 1198 (1974).

[9] J.C. Rife, R.N. Dexter, P.M. Bridenbaugh, and B.W. Veal, Phys. Rev. B **16**, 4491 (1977).

[10] V.V. Sobolev, V.E. Grachev, and S.P. Batanov, J. Appl. Spectroscopy **63**, 221 (1996).

[11] D.E. Aspnes, in *Handbook of Optical Constants of Solids*, Edited by E.D. Palik (Academic, Orlando, 1985), vol. I, p. 89.

[12] S. Adachi, *Optical Constants of Crystalline and Amorphous Semiconductors: Numerical Data and Graphical Information* (Kluwer, Boston, 1999).

[13] D.E. Aspnes, J. Opt. Soc. Am. **70**, 1275 (1980).

[14] G.E. Jellison, Jr. and J.S. Baba, J. Opt. Soc. Am. A **23**, 468 (2006).

[15] S.V. Faleev, M. van Schilfgaarde, and T. Kotani, Phys. Rev. Lett. **93**, 126406 (2004).

[16] S.G. Choi, D.E. Aspnes, N.A. Stoute, Y.D. Kim, H.J. Kim, Y.-C. Chang, and C.J. Palmstrøm, Phys. Stat. Solidi (a) **205**, 884 (2008).

[17] G.S. Solomon, M.L. Timmons, and J.B. Posthill, J. Appl. Phys. **65**, 1952 (1989).

[18] D.E. Aspnes and A.A. Studna, Phys. Rev. B **27**, 985 (1983).

[19] Multilayer analysis, discussed in Sec. IV, suggests that about 9.5 nm of oxide layers (modeled with GeO_2 optical functions) was removed by the chemical treatment.

[20] Y.-D. Kim, S.L. Cooper, M.V. Klein, and B.T. Jonker, Appl. Phys. Lett. **62**, 2387 (1993).

[21] M. van Schilfgaarde, T. Kotani, and S. Faleev, Phys. Rev. Lett. **96**, 226402 (2006).

[22] L. Hedin, Phys. Rev. **139**, A796 (1965).

[23] M. Shishkin, M. Marsman, and G. Kresse, Phys. Rev Lett. **99**, 246403 (2007).

[24] D.E. Aspnes, Thin Solid Films **89**, 249 (1982).

[25] G.E. Jellison, Jr., L.A. Boatner, D.H. Lowndes, R.A. McKee, and M. Godbole, Appl. Opt. **33**, 6053 (1994).

[26] M. Rohlfing and S.G. Louie, Phys. Rev. B **62**, 4927 (2000).

[27] S.D. Yoo and D.E. Aspnes, J. Appl. Phys. **89**, 8183 (2001).

[28] M. Cardona, *Modulation Spectroscopy, Solid State Physics, Suppl. 11*, Edited by F. Seitz, D. Turnbell, and H. Ehrenreich (Academic, New York, 1969).

[29] D.E. Aspnes, in *Handbook of Semiconductors*, Edited by M. Balkanski (North-Holland, Amsterdam, 1980), vol. 2, p. 109.

[30] N.A. Zakharov and V.A. Chaldyshev, Sov. Phys. Semicond. **16**, 763 (1982).

TABLE I. Dielectric function $\varepsilon = \varepsilon_1 + i\varepsilon_2$ of $ZnGeAs_2$ obtained by modeling as described in the text.

E (eV)	ε_1	ε_2
1.5	15.130	2.135
1.6	15.536	2.336
1.7	16.075	2.558
1.8	16.863	2.857
1.9	18.010	3.576
2.0	18.898	5.001
2.1	19.616	6.523
2.2	20.090	8.977
2.3	19.138	11.726
2.4	17.162	13.578
2.5	15.131	14.458
2.6	13.233	14.905
2.7	11.234	14.776
2.8	9.713	13.766
2.9	9.285	12.586
3.0	9.491	12.058
3.1	9.604	12.097
3.2	9.493	12.263
3.3	9.353	12.414
3.4	9.275	12.649
3.5	9.186	13.058
3.6	8.968	13.627
3.7	8.550	14.260
3.8	7.949	14.849
3.9	7.246	15.340
4.0	6.522	15.778
4.1	5.741	16.283
4.2	4.695	16.854
4.3	3.241	17.195
4.4	1.650	16.954
4.5	0.431	16.217
4.6	-0.268	15.508
4.7	-0.869	15.149
4.8	-1.774	14.826
4.9	-2.753	14.115
5.0	-3.392	13.157
5.1	-3.727	12.296
5.2	-3.974	11.581
5.3	-4.200	10.922
5.4	-4.384	10.280
5.5	-4.513	9.661
5.6	-4.587	9.074
5.7	-4.617	8.530
5.8	-4.613	8.030
5.9	-4.588	7.574
6.0	-4.550	7.159

TABLE II. CP energies in eV for $ZnGeAs_2$. Suggested valence- and conduction-band origins for each CP are also listed. For example, the E_4 CP is attributed to transitions from the 16th valence band to the 3rd and 4th conduction bands. Previously reported CP energies are also included for comparison.

CP		E_1	E_2	E_3	E_4	E_5	E_6	E_7	E_8
This work	Exp	2.15 ± 0.01	2.53 ± 0.05	2.68 ± 0.02	3.19 ± 0.02	3.70 ± 0.05	3.94 ± 0.03	4.42 ± 0.01	4.82 ± 0.02
	Cal	2.53	2.88	3.18	3.73	4.15	4.59	5.06	5.46
		$15,16^{VB}\to 1,2^{CB}$			$16^{VB}\to 3,4^{CB}$	$14^{VB}\to 1,2^{CB}$	$13^{VB}\to 1,2^{CB}$ $15^{VB}\to 3^{CB}$	$12^{VB}\to 2^{CB}$ $14^{VB}\to 3,4^{CB}$	$11^{VB}\to 1,2^{CB}$ $15^{VB}\to 5^{CB}$
Ref. 7		2.34	2.50	2.82	3.23	3.76	4.05	4.43	4.80
Ref. 8		2.27	2.43	2.72	3.24, 3.40	3.75	4.07	4.40	
Ref. 10		2.39	2.55	2.68, 2.85	3.10, 3.36	3.60	3.89, 4.17	4.51	4.83
Ref. 9			2.46	2.70	3.24, 3.46		3.80	4.50	4.92
Ref. 6		2.26	2.41	2.74, 2.92	3.23	3.80		4.37	4.92
Ref. 30		2.35	2.42, 2.50	2.68	3.03, 3.30	3.61, 3.68	4.05, 4.22	4.45	

FIGURE CAPTIONS

Figure 1. (a) High-resolution cross-sectional TEM image of a $ZnGeAs_2$ layer grown epitaxially on $In_{0.48}Ga_{0.52}P$ on (001)GaAs. (b) TED pattern taken at the [112] zincblende zone axis of the $ZnGeAs_2$. By comparison to the calculated pattern on the right for chalcopyrite $ZnGeAs_2$ ([111] zone axis for this structure), the extra spots indicated by the arrow show that chalcopyrite-phase $ZnGeAs_2$ has been grown.

Figure 2. **(Color online)** (a) Effects of chemical treatments on $\langle\varepsilon_2\rangle$ for $ZnGeAs_2$. Note that the optical structure is better resolved in the data for the treated sample. (b) XPS spectra of Zn $2p_{3/2}$ peak for $ZnGeAs_2$ acquired for different surface preparations: DI water rinse (solid green line), AmH (a 50 vol. % solution of NH_4OH in DI water) rinse (solid red line), and in-situ Ar sputter cleaned (solid black line). For clarity, the data with AmH treatment and Ar sputtering are offset upward. Inset: XPS spectra showing the C 1*s* peak. The reduction of C-related contamination is clearly seen after AmH treatment.

Figure 3. Electronic energy band structure of $ZnGeAs_2$ calculated in the QS*GW* approximation. The *k*-point labels *T* and *N* correspond to *X* and *L* in the zincblende structure.

Figure 4. **(Color online)** Data (open symbols) and the best-fit curves (solid lines) for Ψ and Δ of $ZnGeAs_2$. Only 20% of the data points are presented to show clearly the quality of fit. Inset: The structure used in the multilayer model.

Figure 5. **(Color online)** (a) Ellipsometric data $\langle\varepsilon_1\rangle$ and $\langle\varepsilon_2\rangle$ (solid black lines) compared to ε_a (dotted red lines) and ε_c (dashed green lines) calculated in the QS*GW* approximation. (b) Detailed comparison between $\langle\varepsilon_2\rangle$ and the calculated $\varepsilon_{\perp 2}$ spectrum from 1.5 to 6.0 eV. Eight critical-point structures are identified and are indicated by arrows. A systematic difference of ~0.5 eV occurs between the CP energies determined from the data and those obtained by calculation due to the simplicity of the calculation.

Figure 6. **(Color online)** Red and blue solid lines: standard CP lineshapes best-fit to second energy derivatives $d^2\langle\varepsilon_1\rangle/dE^2$ (open circles) and $d^2\langle\varepsilon_2\rangle/dE^2$ (open squares), respectively, where $d^2\langle\varepsilon_1\rangle/dE^2$ and $d^2\langle\varepsilon_2\rangle/dE^2$ are calculated as described in the text. For clarity, only half the data points are shown. Energies of each CP are indicated by arrows and labeled following Ref. 7.

Figure 7. **(Color online)** Figures (a) through (f) show **c**ontributions to ε_2 from the 11th through the uppermost 16th valence bands, respectively, calculated in the self-consistent-electronic-structure approximation. The dashed lines show the total contributions from the specific valence bands, for comparison to the overall total shown as the dotted lines. Contributions from the specific valence bands to individual conduction bands are shown as the colored solid lines. Note: The total dielectric function spectrum (dotted curve) appears slightly different from the one shown in Fig. 5, which stems from the difference in the calculation method. The dielectric functions are calculated more accurately by the QSGW approximation (Fig. 5) while the contributions from individual valence band-to-conduction band transitions are better resolved by the self-consistent electronic structure approximation.

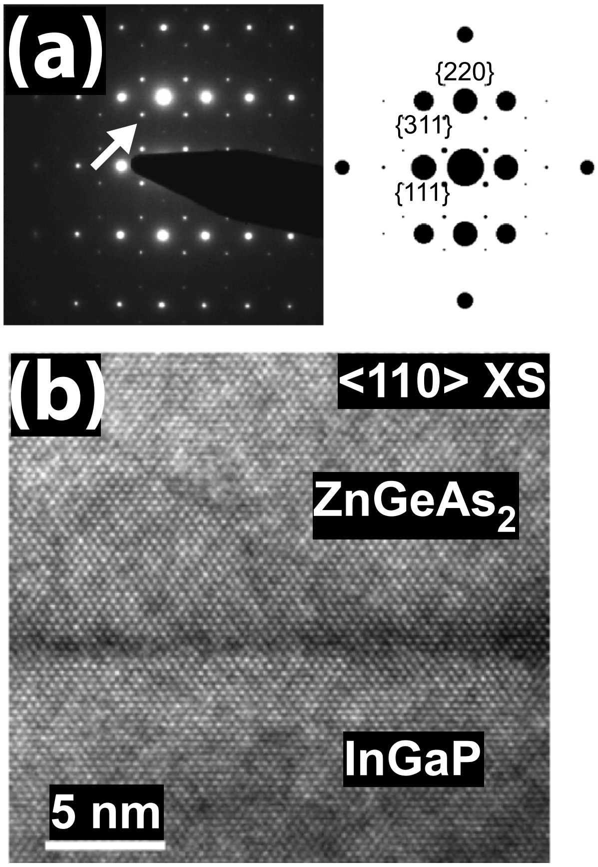

Figure 1 BB11358 25APR2011

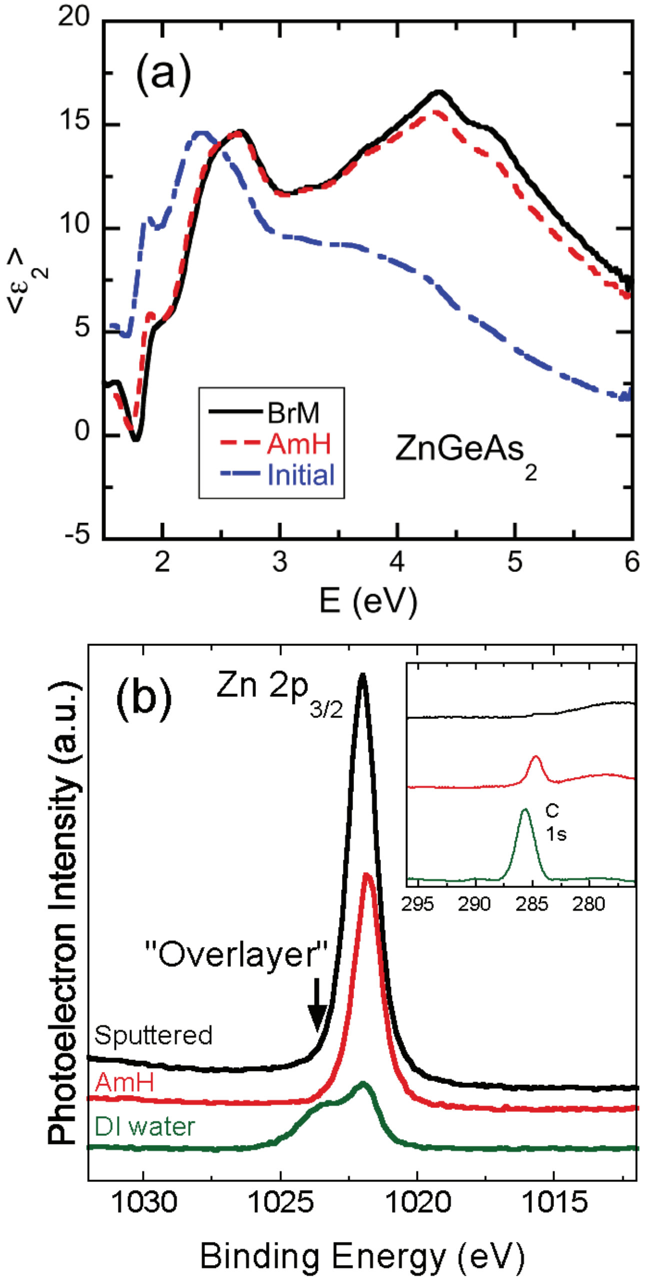

Figure 2 BB11358 25APR2011

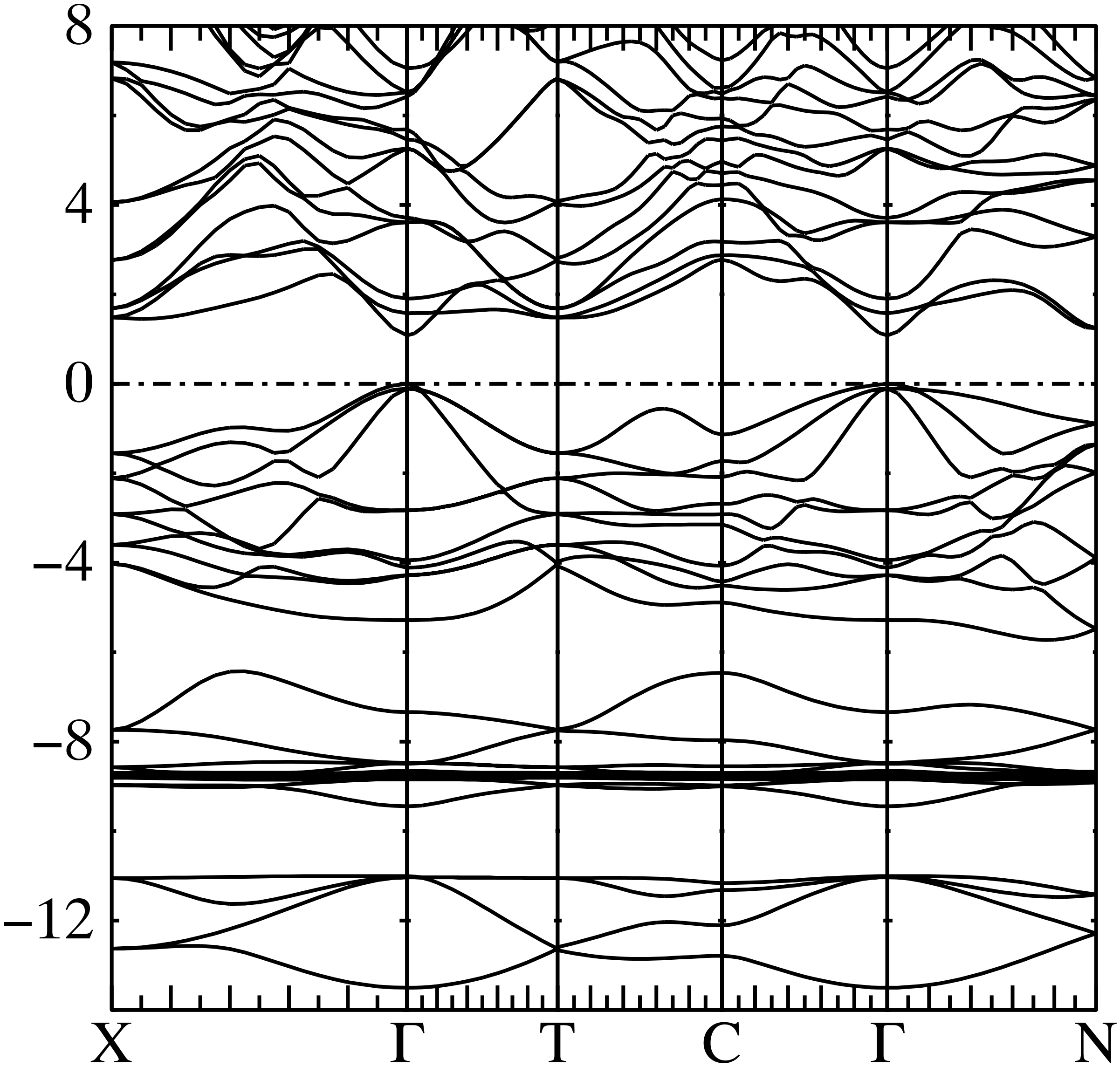

Figure 3 BB11358 25APR2011

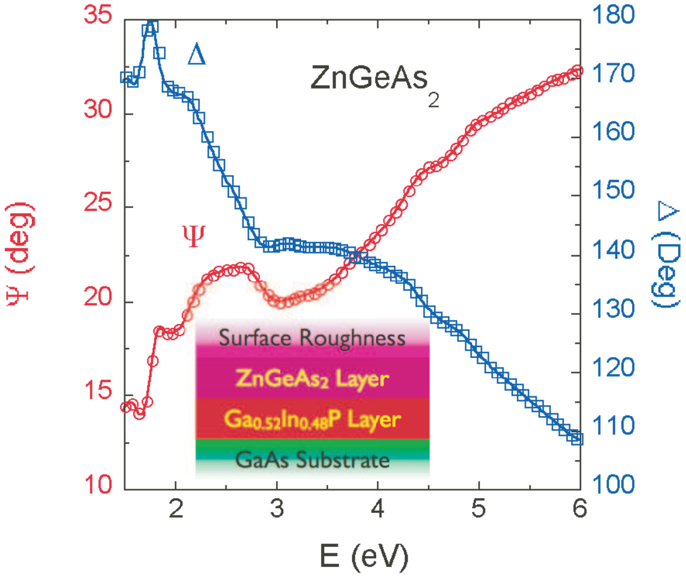

Figure 4 BB11358 25APR2011

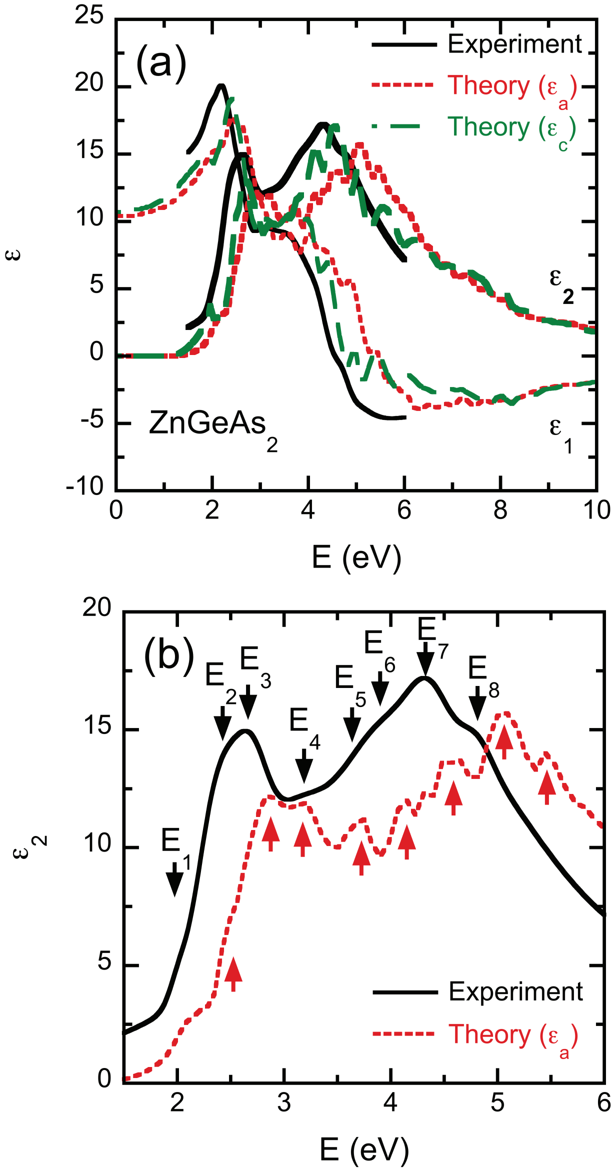

Figure 5 BB11358 25APR2011

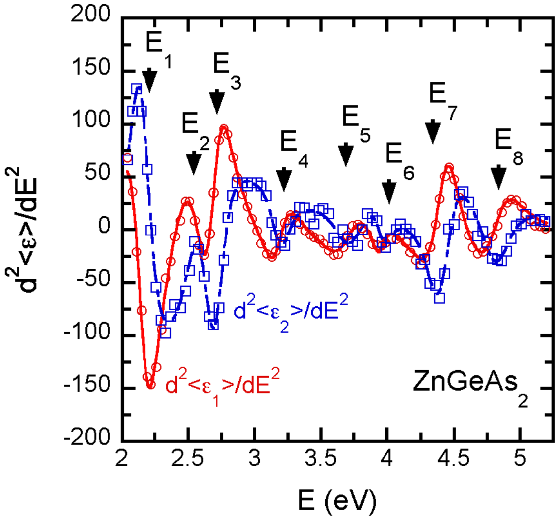

Figure 6 BB11358 25APR2011

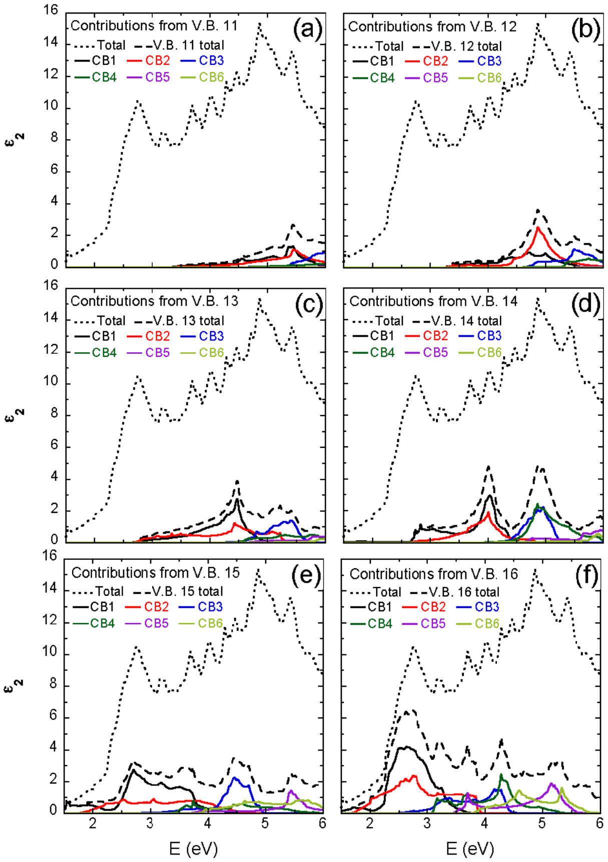

Figure 7 BB11358 25APR2011